NPL REPORT MAT 95

FINITE ELEMENT CALCULATION OF STRESS INTENSITY FACTOR FOR CRACKS DEVELOPING FROM A CORROSION PIT

ALAN TURNBULL AND LOUISE CROCKER

JULY 2020

Finite element calculation of stress intensity factor for cracks developing from a corrosion pit

Alan Turnbull and Louise Crocker

SUMMARY

Finite element analysis (FEA) has been undertaken to calculate the stress intensity factor (K) of cracks emerging from a corrosion pit in a martensitic stainless steel cylinder stressed remotely. The corrosion pit was in the form of a truncated spheroid with depth equal to the full mouth opening. This geometry reflects the configuration found in laboratory testing and in service in low chloride solution, albeit the pit is considered ideally smooth. The pit depth was fixed at 150 μm. A semi-circular crack was adopted with radius ranging from 25 μm to 250 μm. Computations were performed assuming purely elastic condition but the impact of plasticity around the pit was evaluated for selected crack depths.

A key observation of this investigation is that cracks on either side of the pit that are small compared to the pit depth act independently, with K values unaffected by the presence of the other crack. However, as the cracks on either side of the pit grow to a depth approaching the pit depth the K value is mutually increased.

Elastic plastic analysis in discrete cases confirms these trends but highlights the approximate nature of adopting K values that are not strictly applicable because of plasticity around the pit at the applied stress and pit depth investigated.

ISSN 1754 - 2979

https://dio.org/10.47120/npl.MAT95

National Physical Laboratory
Hampton Road, Teddington, Middlesex, TW11 0LW

.

Approved on behalf of NPL by
Dr Gareth Hinds, Science Area Leader, Electrochemistry

CONTENTS

1 INTRODUCTION

In many engineering applications, including aerospace, power plant and offshore structures, environment assisted cracking emanates preferentially from corrosion pits. Corrosion pits create a stress concentration, a relatively aggressive local chemistry, and in the case of growing pits at high applied stress a dynamic plastic strain, all of which individually or in combination can contribute to the development of fatigue or stress corrosion cracks [1]. The application of X-ray computed tomography to 3D imaging of pits and evolving cracks revealed that for many constrained pit geometries, such as hemi-spheroidal or truncated spheroidal shaped pits, cracks do not develop preferentially at the base of the pit as traditionally presumed but closer to the pit mouth [2]. An explanation for this preponderance emerged from finite element analysis (FEA) of the stress and strain around the corrosion pit [1, 3]. At low applied stress, with elastic conditions around the pit, the stress and strain were both maximum around the pit base. However, at high applied stresses (or deep pits at lower stress), plasticity was localised near the pit mouth. In the latter, the stress was distributed more uniformly round the pit but decaying towards the pit mouth. The implication was that the site of initial crack development was better correlated with the localised plastic strain close to the pit mouth.

Since cracks in many cases are developing from a corrosion pit near the pit mouth (appearing like wings on either side of the pit) the question arises as to how to assign a stress intensity factor to cracks emerging from the pit with a depth less than the pit depth. In the absence of detailed FEA, Murakami and Endo [4] approached this empirically and analysed fatigue limits as a function of the size of various defects including pits. They proposed that the stress intensity factor was proportional to the square root of the projected area of the pits and cracks (Figure 1) raised to some power, typically 0.5.

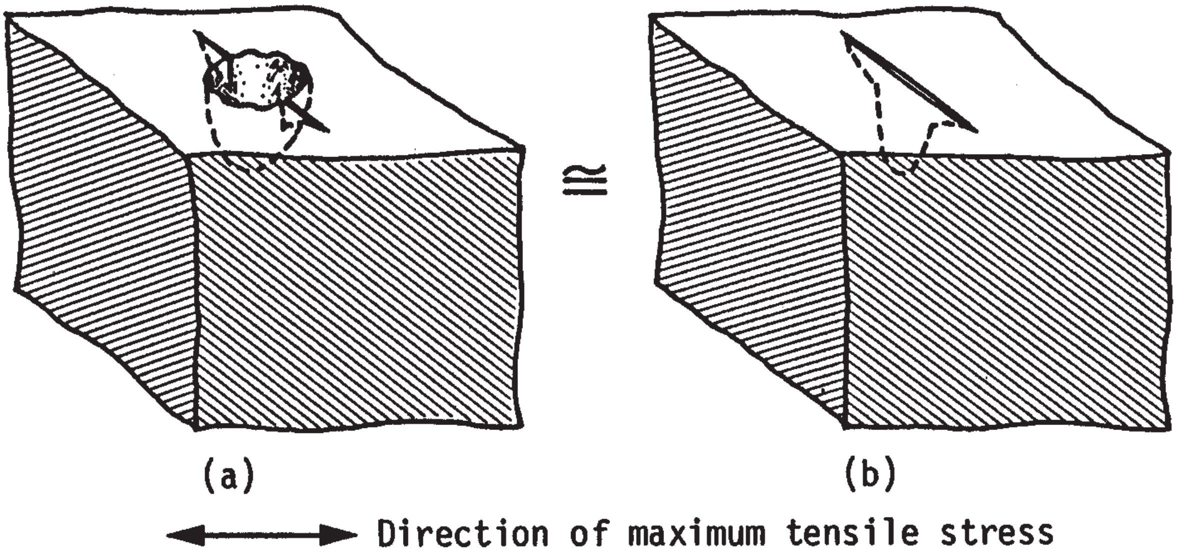

Figure 1: Schematic illustration of the pit with cracks (a) and projected equivalent crack envisaged in approach of Murakami and Endo [4].

This concept did not align well with all data; notably, the dependence of the fatigue limit on pit size for a martensitic stainless steel reported by Zhou and Turnbull [5]. Nevertheless, it highlighted the challenge in defining appropriately the stress intensity factor for a pit with a crack on either side. Should each crack be considered as isolated, with an individual surface length, unconnected to the other crack, or should the two cracks and pit be treated as an effective single crack including the pit, in a manner comparable to the Murakami and Endo approach? Also, if the cracks are not interacting, how does the stress intensity factor change when the cracks merge as the crack depth exceeds that of the pit? To address these questions, FEA was conducted using the truncated spheroidal-shaped pit investigated previously [3], being representative of the macro geometry of pits in martensitic and austenitic stainless steel in chloride environments. No account is taken of microtopographical features that can give rise to local stress concentration [6, 7] and may act as the loci of crack initiation. However, arguably, sustained propagation of such embryonic cracks will depend on the macroscopic stresses and so neglect of these features is not a significant limitation in this analysis.

2 MATERIAL MECHANICAL PROPERTIES

For consistency with previous work, the material adopted was a 12Cr martensitic stainless steel, FV566, that is used extensively for steam turbine blades. The mechanical properties are shown in Figure 2. The test data were derived at 90 °C, corresponding to the typical temperature of first condensation in the low-pressure stage of steam turbines and the temperature adopted for laboratory testing of this steel. The 0.2% proof stress at 90 °C was 820 MPa and the ultimate tensile stress (UTS) was 955 MPa.

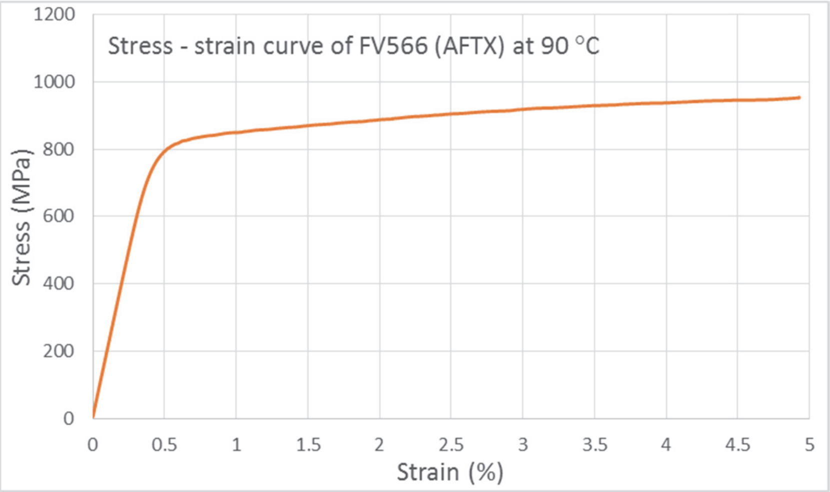

Figure 2: Tensile stress-strain curve for FV 566, 12Cr martensitic stainless steel at 90 °C showing data up to limit of strain gauge measurement, corresponding in this case to the ultimate tensile stress.

3 PIT GEOMETRY

The pit geometry adopted was based on observation of pits in service and in laboratory testing and was best represented by an idealised truncated spheroid with the pit depth equal to the full mouth opening, as represented in Figure 3a. For comparison, a scanning electron microscopy image of a laboratory generated pit is shown in Figure 3b, illustrating the irregularity of the surface at the local level. Such local features can give rise to the microcracks referred to in the Introduction.

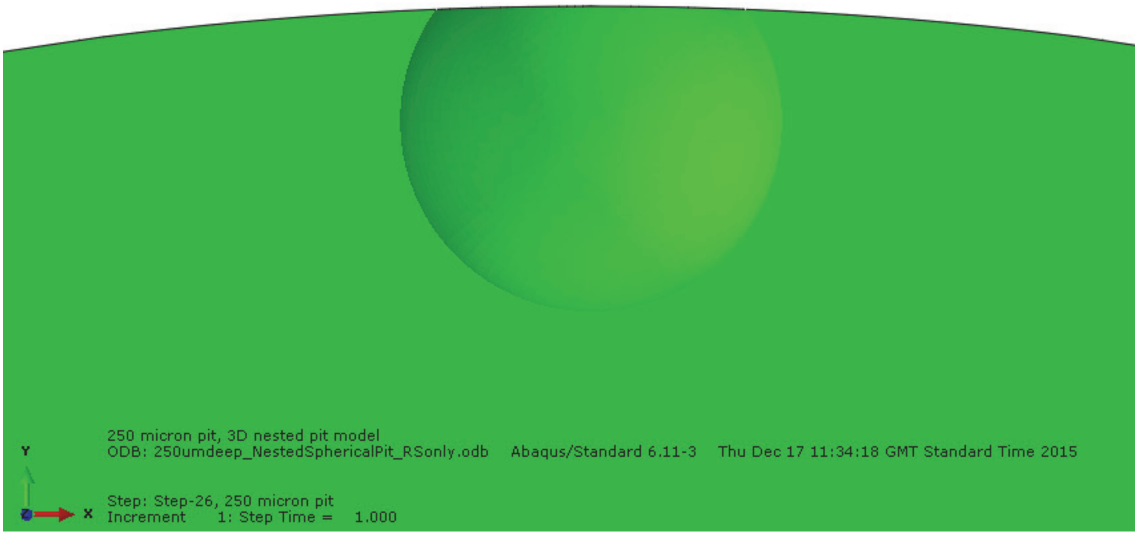

(a)

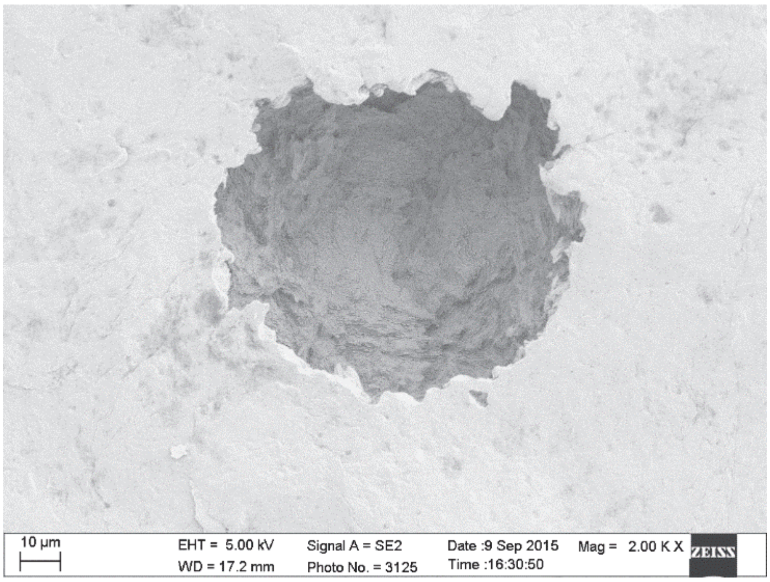

(b)

Figure 3: (a) Example of pit as a smooth truncated spheroid; (b) laboratory grown pit highlighting local microtopographical features.

4 FINITE ELEMENT ANALYSIS

The FEA has been carried out using ABAQUS V6.11-5. A 3-D version of the cylindrical specimen was modelled in the ABAQUS CAE pre-processor. A pit was created half-way along the length of the specimen, as indicated in Figure 4. A uniaxial force is assumed to be applied remotely.

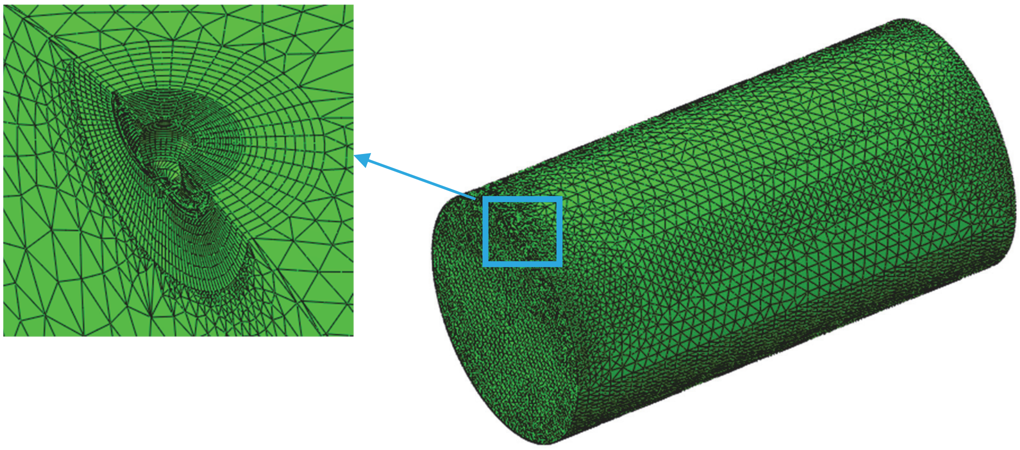

Figure 4: Half-model of specimen geometry showing mesh and refined mesh in the pit region.

The model geometry was partitioned so that a hemispherical region surrounding the pit and crack could be meshed. This allowed a well-controlled, refined mesh of 3D quadratic, reduced integration brick elements to be created to enhance the accuracy of stress prediction. The remainder of the geometry was meshed using a less refined mesh of quadratic tetrahedral elements. Tie constraints were automatically generated on the boundary between the two regions. The mesh configuration associated with pit and cracks of varying depth is shown in Figure 5 (a-f). Note that the stress is into the page. The pit mouth diameter and depth were constant at 150 μm, while the crack was taken to be semi-circular with radius varying from 25 μm to 250 μm. In practice, cracks emerging from pits can vary in geometry depending on the stage of crack development and particularly whether the crack is a fatigue crack or a stress corrosion crack. Here, to address the limited questions posed in this analysis a simple, well-defined, crack shape was adopted. For ease of presentation the scale is not the same for each figure but the constant pit depth of 150 μm acts as an effective benchmark.

For fully-developed cracks, i.e. depth greater than the pit depth, the depth and surface length is defined in the conventional way by the distance from the centre position at the surface to the crack front, whether or not the pit is present. For the semi-circular cracks with a depth smaller than the pit depth the surface length of the crack is measured from the edge of the pit wall and is equated to the crack radius. However, the crack front and crack depth are constrained by the presence of the pit so that for the smaller cracks the surface length is greater than the depth at which the crack intersects the pit. As the crack size approaches that of the pit depth (e.g. a crack of 140 μm) the position of maximum crack depth occurs before the point of intersection.

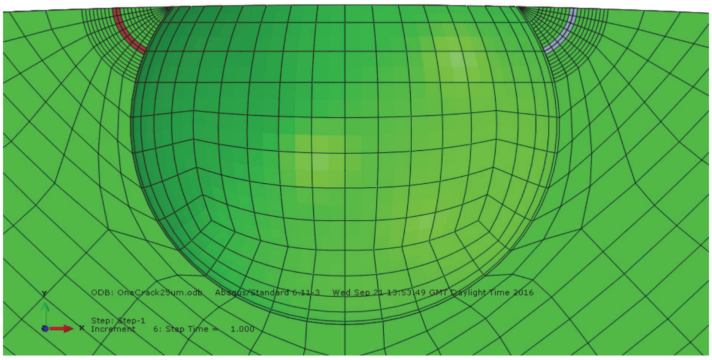

(a) 25 μm

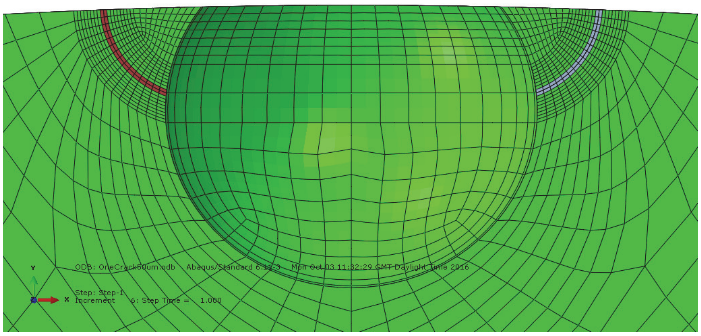

(b) 50 μm

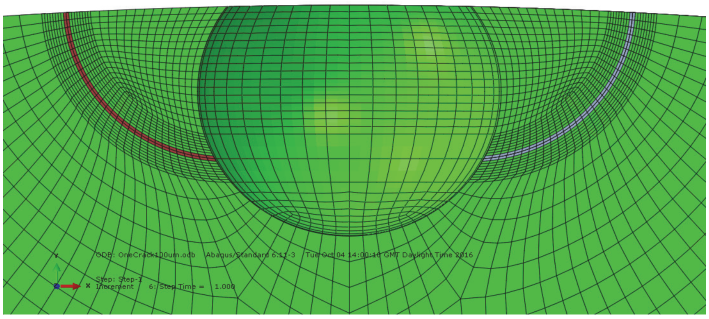

(c) 100 μm

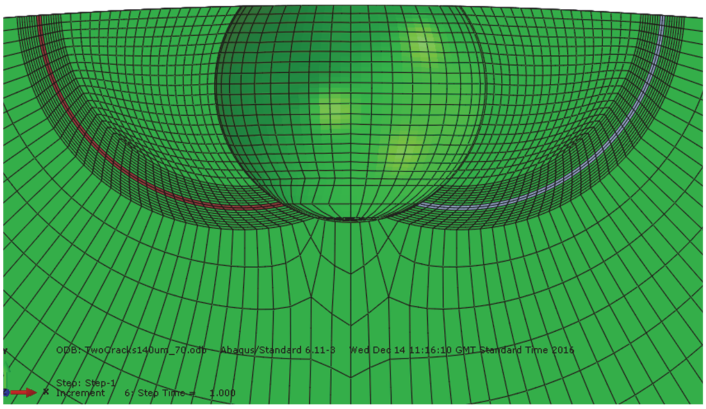

(d) 140 μm

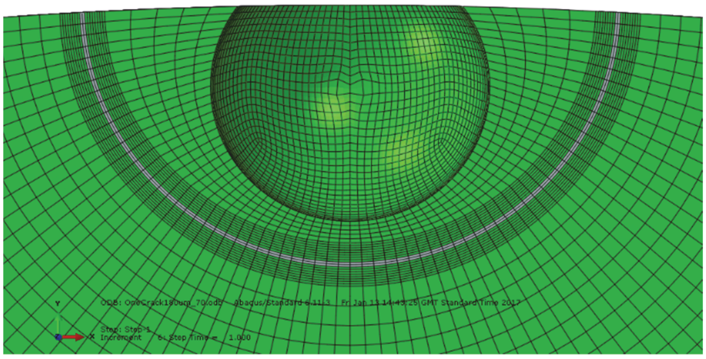

(e) 180 μm

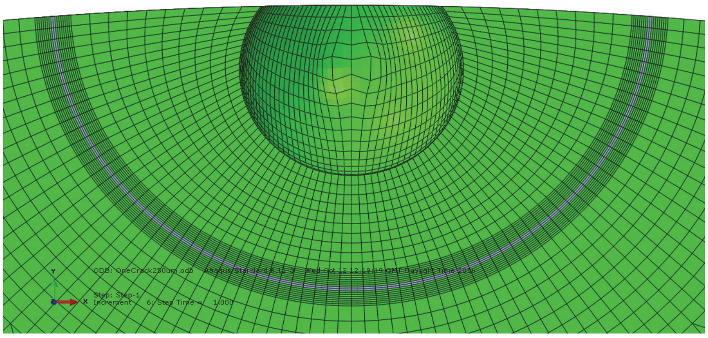

(f) 250 μm

Figure 5. Mesh configuration for pit of constant depth of 150 μm with cracks of varying radius: (a) 25 μm; (b) 50 μm; (c) 100 μm; (d) 140 μm; (e) 180 μm; (f) 250μm.

The contour integral method in Abaqus was used to calculate the stress intensity factor. This approach requires the mesh to be conformed to the crack geometry to explicitly define the crack front and to specify the virtual crack extension direction. Multiple contour integral evaluations can be obtained at each location along the crack. Each contour is a ring of elements completely surrounding the nodes along the crack line from one crack face to the opposite crack face. Each contour provides an evaluation of the contour integral.

In this model the geometry has been partitioned to map 9 'rings' of elements around the crack tip, see Figure 6, providing 9 contour integral evaluations at each node along the crack in order to obtain contour-independent results. At the crack line, the model uses brick elements with a collapsed side to create wedge-shaped elements which introduce a singularity at the crack tip. A square root singularity was defined at the crack tip as a linear elastic, small-strain analysis was being used. An alternate 1/r singularity can be defined for the cases where plasticity is included but for these models there is very little difference in J values predicted using the two definitions.

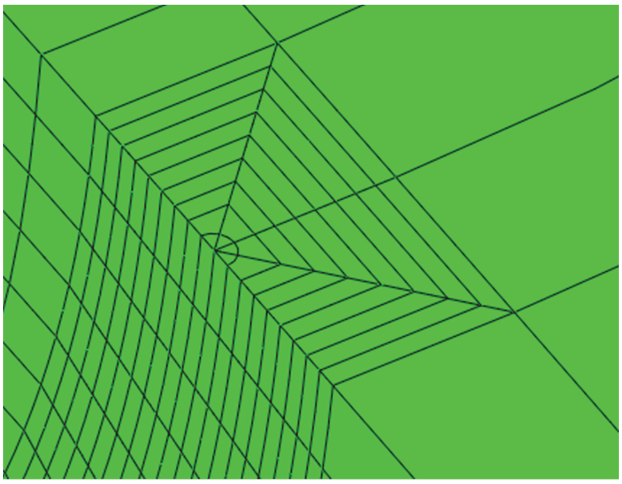

Figure 6. Controlled mesh around the crack tip showing the 9 contour 'rings' including the wedge elements at the crack tip.

As can be seen in Figure 4, a half model has been used to reduce the computational time. A plane of symmetry was defined along the crack plane and the change in potential energy calculated from the virtual crack front advance is automatically doubled to compute the correct contour integral values. In the model the crack face itself is not included in the symmetry plane definition.

Stress intensity factor values were output for each contour integral at each point along the crack line. When outputting the results, data from the first contour were excluded as the first contour is influenced by the singularity associated with the crack tip. For 3D models with an open crack front, outputs may be inaccurate from node sets at the crack front ends. This resolution difficulty is compounded by the skewness of the outermost layer of elements, but the effect is confined only to the contour integrals at the front ends. In this model average stress intensity factor values have been obtained from nodes along the central crack length region, away from the crack front ends. For FE analyses that include plasticity the calculation of stress intensity factor values is not appropriate, so the J integral was output instead.

5 RESULTS AND DISCUSSION

The analysis was undertaken primarily assuming full elastic behaviour as K is most commonly used in defining the mechanical driving force associated with cracks from pits despite its limitation upon macroscopic yielding at the pit. Hence, while stress concentration would ensue in response to the pit in the elastic model, any limit and redistribution of stress due to the onset of plasticity would not be accounted for. To address that possibility, computations were also undertaken with plasticity incorporated, with the J-integral as the parameter defining the mechanical driving force [8, 9].

The goal was not to estimate K, or J, for every possible configuration of both pit and crack size but simply to address the more limited query of the extent to which the stress intensity factor depends on the presence of the pit and whether a crack of depth smaller than the pit depth on one side of the pit affects in any way the stress intensity factor of a small crack on the other side. In other words, are the cracks behaving independently, and what happens as they merge towards a single crack? Computations of the stress intensity factor were undertaken assuming a single pit depth of 150 μm, with the crack radius varying from 25 μm to 250 μm and applied stresses of 70% $\sigma_{0.2}$ and 90% $\sigma_{0.2}$. Since the trend in results was broadly similar for both applied stresses, FE predictions for the latter only are reproduced in the main text but some data for 70% (based solely on elastic theory) are appended. In the steam turbine blade application that formed the basis of this analysis, the stresses in service are typically about 90% $\sigma_{0.2}$.

Contour plots of the stress distribution for the elastic and elastic-plastic case for a crack of depth 140 μm (crack on either side of pit) are shown in Figures 7 and 8. For clarity only one half of the pit is shown, taking into account the symmetry of the system. The stress axis is perpendicular to the crack front. The stress profiles are broadly similar except for the reduced localisation of stress around the base of the pit for the elastic-plastic case. This is not unexpected as yielding would constrain the attainable stress in the latter; note the 0.2% proof stress is 820 MPa. Accordingly, a purely elastic solution for K may overestimate the value but should not affect the relative comparison.

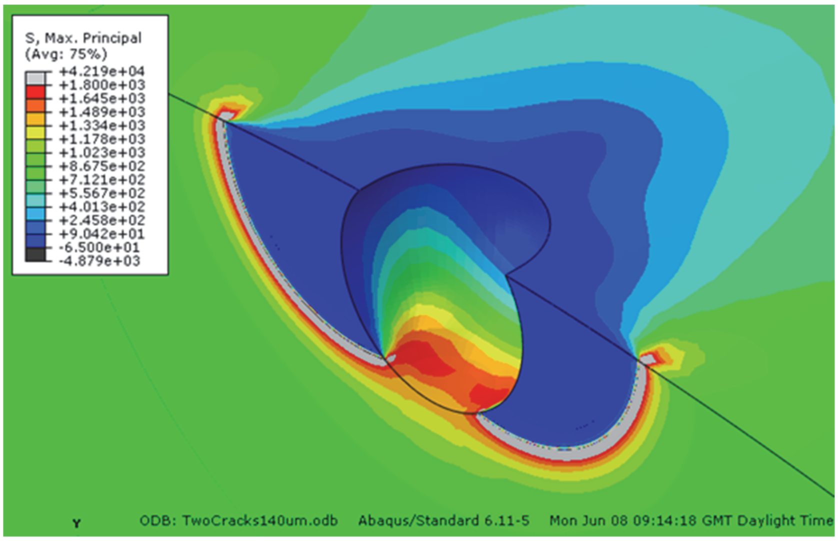

Figure 7. Stress distribution (in MPa) around pit and 140 μm deep crack calculated assuming pure elastic conditions. Remote stress applied is 90% $\sigma_{0.2}$.

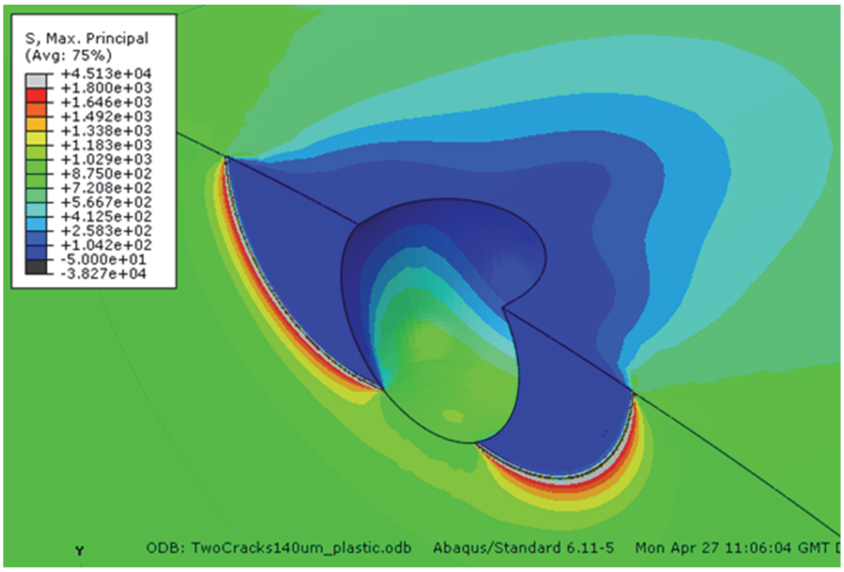

Figure 8. Stress distribution (in MPa) around pit and 140 μm deep crack calculated assuming elastic-plastic conditions. Remote stress applied is 90% $\sigma_{0.2}$.

The calculated K distribution along the crack front at 90% $\sigma_{0.2}$ is shown in Figure 9 for the 25 μm crack, assuming either a crack on one side of the pit or a crack on both sides, and in Figure 10 for the 140 μm crack. Note that K_I refers to a Mode 1 crack, pure opening mode. The crack front number refers to a discretised distance (determined by the number of nodes) along the crack front from the intersection with the pit to the specimen surface. The crack front number has been presented as a normalised value to allow direct comparison between models with slight variations in meshes (and hence number of nodes) along the crack front. The K values at the two extremes, pit wall surface and sample surface, will be affected by the discontinuity in material and generate artificial results that are physically unrealistic. This is more apparent at the interface with the corrosion pit. Otherwise, the K value is relatively uniform along the crack front with a slight increase in value towards the boundaries.

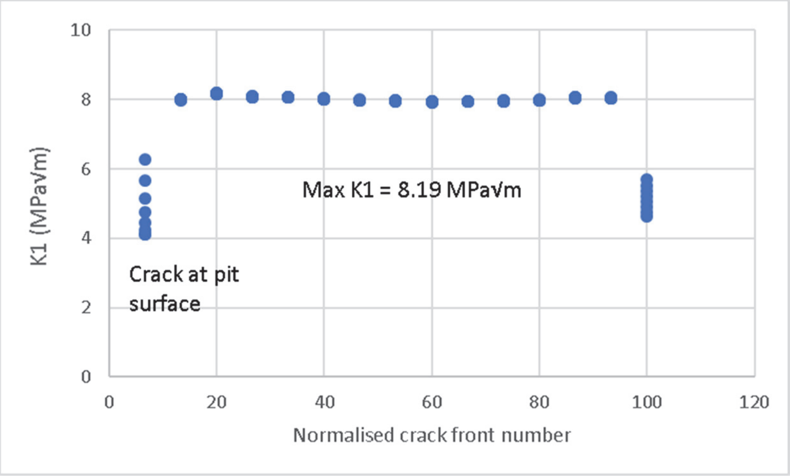

(a)

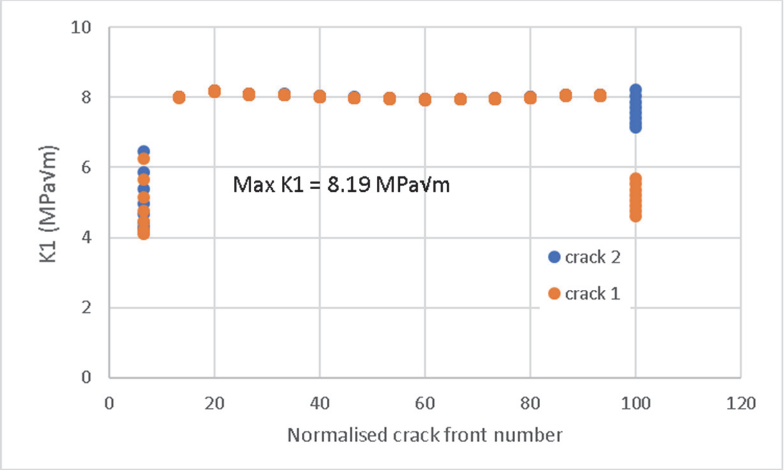

(b)

Figure 9. Distribution of the stress intensity factor along the crack front for crack of radius 25 μm (surface length measured from the intersection with the pit) at an applied stress of 90% $\sigma_{0.2}$ assuming elasticity only; (a) single crack, (b) crack on each side of pit.

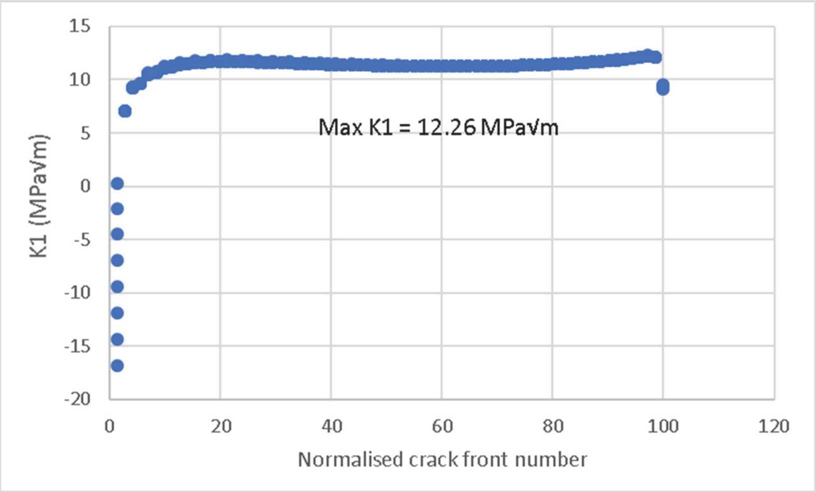

(a)

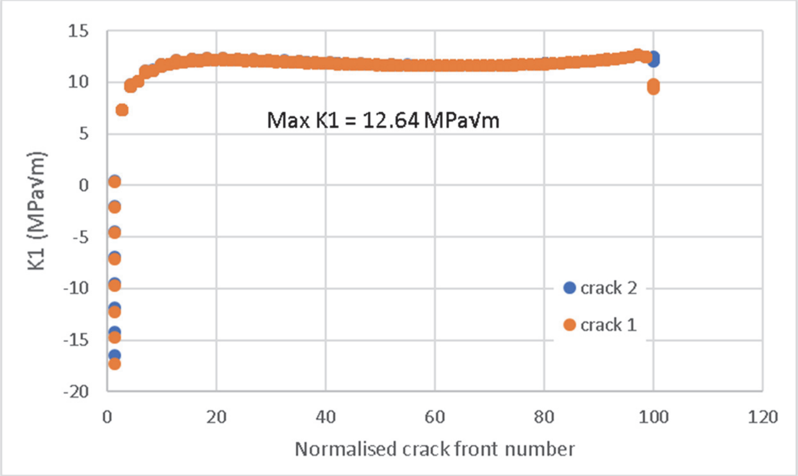

(b)

Figure 10. Prediction of the distribution of the stress intensity factor along the crack front for crack of radius 140 μm at an applied stress of 90% $\sigma_{0.2}$ assuming elasticity only; (a) single crack, (b) crack on each side of pit.

When the crack is deeper than the pit but close to the pit base at its maximum depth there is a dip in the predicted K value towards the base of the pit compared to the situation with no pit, as shown for the 180 μm crack in Figure 11. For a purely elastic solution this is a surprising result, insofar as a reduction in local elastic stress due to the pit is not envisaged, yet does not seem to be an artefact. A conceptual explanation is not readily forthcoming.

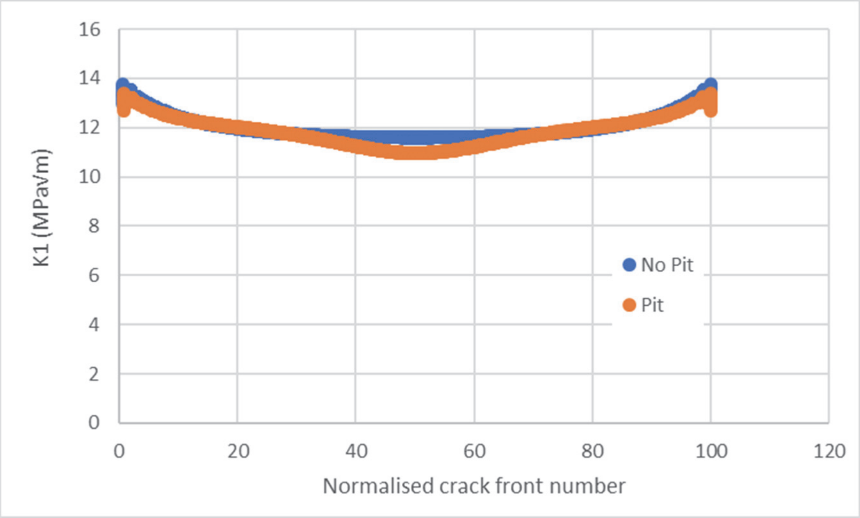

Figure 11. Prediction of the distribution of the stress intensity factor along the crack front for crack of radius 180 μm at an applied stress of 90% $\sigma_{0.2}$ assuming elasticity only.

Table 1 summarises the K values calculated for each crack radius, averaged over the crack front but neglecting the distortions at the interface with the pit wall and the surface. The significant increase in the K value due to the presence of the pit is readily apparent for the 25 μm crack, although the predictions for K for the 180 μm crack seem anomalous (and not consistent with calculations based on the J-integral). It is also evident that the K value for a crack of radius less than the pit depth is only marginally influenced by the presence of a crack on the other side of the pit when the crack is small. However, the tendency for an increase in K in response to the presence of the other crack becomes more discernible as the crack radius approaches the pit depth; for example, at a crack radius of 140 μm. At this depth, the presence of the crack begins to exert an influence on the stress distribution around the base of the pit and thus impacts on the other crack.

The focus on the K values and an elasticity-based model reflects the predominant use of K to characterise the mechanical driving force for cracks emerging from pits in most of the literature, but its limitations for deep pits at elevated stresses are well-recognised if sometimes ignored for pragmatic reasons. Nevertheless, it is essential to ascertain whether the same trends would be predicted based on a more rigorous elastic-plastic analysis. Accordingly, calculation of the J-integral was conducted for cracks of with radius ranging from very small compared to the pit depth to significantly deeper than the pit. The results are expressed also in Table 1.

It is evident from Table 1 that the same conclusions with respect the mechanical driving force for the single crack versus two cracks prevail. Most notable is the significant decrease in J integral when comparing the values for the 140 μm crack with those for the deeper 180 μm crack highlighting the influence of the pit and the significant gradient in mechanical driving force. For the deepest crack, of depth 250 μm, the mechanical driving force for the crack is determined by the elastic field around the pit with the effect of the pit being small. Hence, the J-integrals are similar for both the purely elastic and elastic-plastic analysis.

Table 1. FE calculated values for K and J-integral for cracks (averaged over crack front except anomalous end values) associated with 150 µm deep pit (unless specified otherwise) with applied stress of 90% $\sigma_{0.2}$. A full elastic solution has been adopted except where noted.

Crack radius /µm	Configuration		K/MPa.m$^{0.5}$	J-integral/ MPa m
25	single crack	RH crack	8.02	
	single crack NO PIT	RH crack	4.34	
	single crack elastic-plastic	RH crack		4.33×10^{-4}
	single crack elastic-plastic NO PIT	RH crack		2.24×10^{-4}
	two cracks	RH crack	8.03	
		LH crack	8.03	
50	single crack	RH crack	9.57	
	two cracks	RH crack	9.60	
		LH crack	9.61	
100	single crack	RH crack	10.78	
	two cracks	RH crack	10.96	
		LH crack	10.95	
140	single crack	RH crack	11.51	
	two cracks	RH crack	11.89	
		LH crack	11.90	
	single crack elastic-plastic	RH crack		8.34×10^{-4}
	two cracks elastic-plastic	RH crack		9.01×10^{-4}
		LH crack		9.03×10^{-4}
180	single crack	full crack	11.57	
	single crack NO PIT	full crack	11.78	
	single crack elastic-plastic	full crack		9.37×10^{-4}
	single crack elastic-plastic NO PIT	full crack		8.82×10^{-4}
250	single crack	full crack	13.99	
	single crack NO PIT	full crack	13.90	
	single crack elastic plastic	full crack	13.98*	1.24×10^{-3}
	single crack elastic-plastic NO PIT	full crack		1.25×10^{-3}

** K value calculated from J-integral for comparison – valid for this case.*

6 CONCLUSIONS

Finite element analysis to determine the stress intensity factor of cracks emerging from pits in a martensitic stainless steel at remote stress of 90% $\sigma_{0.2}$ demonstrates that single cracks on either side of the pit do not interact with each other in determining their respective K values until the crack depth approaches that of the pit depth.

While this conclusion is not dependent on the approximate elastic analysis adopted when calculating K, the unconstrained stresses in response to the neglect of local plasticity around the pit at these high applied stress levels will lead to erroneous predictions of the absolute value

More rigorous elastic-plastic analysis indicates the constraints induced by local yielding on the attainable stresses around the pit and the limitation in using K. Nevertheless, the trend in response to crack interaction on either side of the pit is similar as is the effect of the pit in elevating the mechanical driving force along the crack front.

7 ACKNOWLEDGEMENTS

This research was supported by the National Measurement System of the Department of Business, Energy and Industrial Strategy.

8 REFERENCES

1. A. Turnbull, L. Wright and L. Crocker, New insight into the pit-to-crack transition from finite element analysis of the stress and strain distribution around a corrosion pit, Corros. Sci., 52 (2010) 1492-1498.
2. D. A. Horner, B. J. Connolly, S. Zhou, L. Crocker, and A. Turnbull, Novel images of the evolution of stress corrosion cracks from corrosion pits, Corros. Sci, 53 (2011) 3466-3485.
3. A. Turnbull and L. Crocker, Finite element analysis of the effect of pit shape on the local stress and strain distribution, NPL Report MAT 51, 2011.
4. Y. Murakami and M. Endo, Effect of hardness and crack geometries on ΔK_{th} of small cracks emanating from small defects, Proceedings of The Behaviour of Short Fatigue Cracks, eds. K.J. Miller and E.R. de los Rios, EGF 1, EGF Publication 1, Fatigue of Engineering Materials Limited, 1986, University Press, Cambridge, pp 275-294.
5. S. Zhou and A. Turnbull, Influence of pitting on the fatigue life of a turbine blade steel, Fatigue & Fracture of Engineering Materials & Structures, 22 (1999) 1083-1091.
6. J.T. Burns, J.M. Larsen and R.P. Gangloff, The effect of initiation feature on microstructure-scale crack propagation in Al-Zn-Mg-Cu, Int. J. Fatigue, 42 (2012) 104-121.
7. L. Wright and A. Turnbull, FE analysis of stress and strain localisation associated with microtopographical features in corrosion pits, NPL Report MAT 78, 2015.
8. G.P. Cherepanov, The propagation of cracks in a continuous medium, J. Appl. Maths. and Mechs., 31 (1967) 503-512.
9. J.R. Rice, A path independent integral and the approximate analysis of strain concentration by notches and cracks, J. Appl. Mechs., 35 (1968) 379-386.

10 APPENDIX

This appendix summarises in Table A1 the key data computed for an applied stress of 70% of $\sigma_{0.2}$, assuming purely elastic behaviour.

The K values in parentheses are calculations based on a full model rather than the half-cylinder model and symmetry assumption (see Section 4). The differences are sufficiently small to justify adoption of the computationally more efficient half-cylinder model.

Table A1. FE calculated values for K for cracks (averaged over crack front except anomalous end values) associated with 150 μm deep pit with applied stress of 70% $\sigma_{0.2}$.

Nominal crack depth/μm	Configuration		$K/MPa.m^{0.5}$
25	single crack	RH crack	6.24
	two cracks	RH crack	6.24
		LH crack	6.25
50	single crack	RH crack	7.44 (7.45)
	two cracks	RH crack	7.47 (7.48)
		LH crack	7.47 (7.48)
100	single crack	RH crack	8.38
	two cracks	RH crack	8.53
		LH crack	8.53
140	single crack	RH crack	8.97
	two cracks	RH crack	9.25
		LH crack	9.26
180	single crack	full crack	9.00
180	single crack NO PIT	full crack	9.16
250	single crack	full crack	10.88
250	single crack NO PIT	full crack	10.88